Author Manuscript
Accepted for publication in a peer-reviewed journal

NIST National Institute of Standards and Technology • U.S. Department of Commerce

Published in final edited form as:
Nat Catal. 2019 ; 2: . doi:10.1038/s41929-019-0328-1.

Supported Catalyst Deactivation by Decomposition into Single Atoms Is Suppressed by Increasing Metal Loading

Emmett D. Goodman[1], **Aaron C. Johnston-Peck**[2], **Elisabeth M. Dietze**[3], **Cody J. Wrasman**[1], **Adam S. Hoffman**[4], **Frank Abild-Pedersen**[1,4], **Simon R. Bare**[4], **Philipp N. Plessow**[3], **Matteo Cargnello**[1,*]

[1]Department of Chemical Engineering and SUNCAT Center for Interface Science and Catalysis, Stanford University, Stanford, CA 94305, USA

[2]Material Measurement Laboratory, National Institute of Standards and Technology, Gaithersburg, Maryland, 20899, USA

[3]Institute of Catalysis Research and Technology, Karlsruhe Institute of Technology, Hermann-von-Helmholtz-Platz 1, D-76344 Eggenstein-Leopoldshafen, Germany

[4]Stanford Synchrotron Radiation Lightsource, SLAC National Accelerator Laboratory, 2575 Sand Hill Rd., Menlo Park, CA 94025, USA

Abstract

In the high-temperature environments needed to perform catalytic processes, supported precious metal catalysts severely lose their activity over time. Even brief exposure to high temperatures can lead to significant losses in activity, which forces manufacturers to use large amounts of noble metals to ensure effective catalyst function for a required lifetime. Generally, loss of catalytic activity is attributed to nanoparticle sintering, or processes by which larger particles grow at the expense of smaller ones. Here, by independently controlling particle size and particle loading using colloidal nanocrystals, we reveal the opposite process as a novel deactivation mechanism: nanoparticles rapidly lose activity by high-temperature nanoparticle decomposition into inactive single atoms. This deactivation route is remarkably fast, leading to severe loss of activity in as little as ten minutes. Importantly, this deactivation pathway is strongly dependent on particle density and concentration of support defect sites. A quantitative statistical model explains how for certain reactions, higher particle densities can lead to more stable catalysts.

Increased catalyst stability, especially in automotive emissions control applications, is of paramount importance in order to decrease the loading of rare and precious noble metals[1,2].

[*]Corresponding author: mcargnello@stanford.edu.

Author Contributions.

E. D. G. and M. C. conceived and designed the experiments. E. D. G. performed catalyst synthesis and testing. A. J.-P. performed HAADF-STEM characterization. E. D. performed DFT calculations with support from P. P. C.W. performed XAS analysis with support from A. H. and S. B. F. A.-P. contributed in discussion of atomic energetics. E. D. G. and M. C. wrote the manuscript with contributions and discussions from all authors.

Competing Interests.

The authors declare no competing interests.

Additional Information. Reprints and permissions information are available online. Readers are welcome to comment on the online version of the paper. Correspondence and requests for materials should be addressed to M.C. (mcargnello@stanford.edu)

Unfortunately, due to declining catalytic activity throughout operation, emissions control catalysts are loaded with up to ten grams of precious metals to ensure effective catalysis over the desired lifetime[3,4]. Two mechanisms are universally proposed for the loss of reactive surface area: particle migration and coalescence, and atomic (or Ostwald) ripening. The former involves the movement and coalescence of entire nanoparticles, while the latter involves the motion of atomic species from smaller to larger particles. In both mechanisms, researchers observe an emergence of larger particle aggregates, a clear indication of particle sintering, which is correlated with the corresponding loss of activity. Although difficult to distinguish between sintering processes, researchers aim to create nanostructures that maximize distances between catalytic nanoparticles in hopes of minimizing particle growth[5–7]. Although it is very challenging to isolate a specific deactivation mechanism, clear understanding of specific catalyst degradation mechanisms is important for the rational design of stable heterogeneous catalysts[8–10].

In this work, instead of catalyst deactivation due to particle growth, we identify and explore the novel deactivation mechanism of nanoparticle decomposition into inert single atoms. Importantly, the extent and severity of this deactivation mechanism is a direct function of nanoparticle size and spatial arrangement. However, using traditional catalyst synthesis techniques, the spatial arrangement of particles and its influence on catalyst properties are difficult to control and study, as catalyst metallic loading and particle size are two strongly connected parameters. Here, utilizing colloidal nanocrystals to independently control particle size and particle loading - two parameters crucial to catalyst stability - we demonstrate an unexpected result: higher particle loadings can result in a more stable catalyst.

RESULTS AND DISCUSSION

Independent control of particle size and loading

In this work we study Pd catalysts because of their relevance in emission control catalysis, but we anticipate this observation to be of general validity and interest in multiple supported systems. In order to vary nanoparticle density without affecting particle size, different amounts of the same 7.9±0.6 nm preformed colloidal Pd nanoparticles (NPs) were added to the same mass of stabilized gamma-alumina (γ-Al_2O_3) support to obtain catalysts with a Pd loading of 0.659 wt. %, 0.067 wt. %, and 0.007 wt. %. These loadings corresponded to a dense, intermediate, and sparse NP density on the support (Fig. 1a–c, Supplementary Fig. 1). Note that before NP impregnation, the γ-Al_2O_3 support was calcined at 900 °C for 24 h to ensure that the support would be stable throughout our aging experiments, which were generally performed at lower temperatures for much shorter durations. Organic ligands were removed from the particle surfaces via rapid heating treatment[11], leaving the original NP size uniformity unchanged (Supplementary Fig. 2). High-angle annular dark-field scanning transmission electron microscopy (HAADF-STEM) characterization demonstrates the random distribution of Pd NPs on the alumina support and the control over particle loading and density. An obvious change in NP density is observed as the overall Pd mass loading on alumina is varied, leading to average NP density of 22, 2.2 and 0.23 NPs per square micron for dense, intermediate and sparse samples, respectively. These values correspond to average

interparticle distances of 1100 nm, 340 nm and 110 nm for the three samples, respectively, according to Monte Carlo simulations paired with Voronoi analyses (Supplementary Table 1, Supplementary Fig. 3). Based on characterization and simulation, we conclude that these materials represent a set of powder catalysts with identical NP size yet different nanoparticle spatial arrangements.

We set out to compare the thermal stability of these systems using methane combustion as a probe reaction, because this reaction requires stable materials that can withstand high temperatures for emissions control applications[4,12]. Additionally, methane combustion is a useful probe reaction because combustion rates are proportional to exposed Pd surface area, so combustion activity is a good proxy for exposed reactive surface area[13,14]. The protocol to measure catalyst deactivation included a measurement of catalytic activity at 460 °C (a temperature where Pd is unaffected by water poisoning[15]), in-situ aging in dilute oxygen at 775 °C for 1 h, and a subsequent measurement of catalytic activity at 460 °C in the same reaction mixture as before (Fig. 1d). Stable materials would show the same conversion before and after the aging treatment, but unstable materials would show decreased conversion after the aging treatment. Although this process is an approximation of realistic conditions, it allows for isolation of the environmental conditions responsible for catalyst deactivation. The mass of each catalyst and Al_2O_3 diluent was chosen as to load the same amount of Pd into the reactor, while keeping the total bed volume constant. Before the aging treatment, each test showed similar CH_4 conversion (~85%), indicating no significant low-temperature interaction between Pd nanoparticles (Fig. 1d–e). Conventional wisdom would predict that the catalyst with lowest Pd particle density should be the most stable, due to a lower probability of particle migration and coalescence or interparticle atomic exchange. Surprisingly, after high-temperature aging the dense Pd/Al_2O_3 catalyst showed completely stable activity, while the sparse Pd/Al_2O_3 catalyst showed dramatic deactivation, with conversion decreasing from 85% to 20%. Interestingly, the intermediate sample showed an intermediate loss of activity to about 55% conversion after the aging treatment. Counterintuitively, while the most isolated Pd nanoparticles lost nearly all their combustion activity, the Pd/Al_2O_3 sample with the highest particle density remained stable.

Density-dependent decomposition of nanoparticles into single atoms

The surprising catalytic stability of the dense Pd/Al_2O_3 material was confirmed via HAADF-STEM (Fig. 2a, Supplementary Fig. 4). Comparing particle size distributions before and after aging in oxygen demonstrates lack of particle agglomeration (Fig. 2a,d), although the peak in particle size shifted to 9.3 nm due to oxidation of Pd to PdO, and a population of smaller particles was formed. In the case of the intermediate and sparse density catalysts, HAADF-STEM reveals the presence of Pd species in the form of Pd clusters distinctly smaller than the original 7.9 nm particles (Fig. 2b–c,e–f). However, the intermediate material still shows a fraction (10%) of larger nanoparticles, particularly in areas of high nanoparticle density (Supplementary Fig. 4), whereas only one single nanoparticle larger than 4 nm was observed in the sparse sample. A similar density-dependent stability was found when aging the materials under methane combustion conditions instead of just oxygen. In this case, direct observation of Pd single atoms was possible (Supplementary Fig. 5).

Extended x-ray absorption fine structure (EXAFS) confirms the HAADF-STEM findings: for the sparse catalyst, the Pd-Pd coordination contribution disappears after aging, and the average first shell Pd-Pd coordination number approaches zero, significantly less than that for bulk Pd or PdO (12 or 4, respectively) (Fig. 2h and Supplementary Table 2). X-ray photoelectron spectroscopy (XPS) confirms that although dense and sparse Pd catalysts both start off in the same metallic Pd state, the sparse catalyst evolves towards a highly disperse and highly oxidized state, characterized by a binding energy ~1 eV higher than bulk PdO[16] (Fig. 2g). Inductively coupled plasma mass spectrometry (ICP-MS) quantitatively shows that all Pd is conserved after the aging treatment and that none is lost to the gas phase (Supplementary Table 3). The fact that Pd could be dissolved for ICP analysis while the bulk of Al_2O_3 remains intact further suggests that Pd is still located on the Al_2O_3 surface and did not enter the support lattice. Taken together, the data suggests that at low Pd density, NPs decompose in single atomic species, while at denser particle loadings, catalysts maintain their size and particle dispersion.

If deactivation was due to either particle migration and coalescence or classic atomic ripening processes, as traditionally posited in the case in high-temperature applications, an increase of particle size would be expected[17]. The emergence of smaller particles suggests that atomic processes are still active, but instead of Pd atoms moving from smaller to larger particles, Pd atoms are stabilized by the support, leading to atomically dispersed species. Importantly, the single-atoms that form are much less active for the methane combustion reaction, likely due to the need of a critical ensemble size to adsorb oxygen and fully dehydrogenate methane. This data sheds new light onto the poor activity of single atom catalysts for hydrocarbon combustion, an important result in the fiercely debated area of single-site catalysis. Although single atoms are rarely described on pure γ-Al_2O_3 (i.e. compared to reducible oxides such as CeO_2 or Fe_2O_3), recent works have identified the stability of atomically dispersed Pt on Al_2O_3[18,19]. Stabilization of atomically dispersed Pd has been identified before, but on $Ce_xZr_{1-x}O_2$-Al_2O_3 and La-Al_2O_3 supports which are purported to stabilize atomic species[20,21]. Here, we report that at low nanoparticle densities, complete decomposition of 7.9 nm particles, consisting of ~18,000 atoms, into stable single atom species on unmodified, commercial Al_2O_3 is obtained. Although the same previous reports demonstrate Pd atomic species as good CO oxidation catalysts, we here show that these species are very poorly active for CH_4 combustion and the main cause of catalyst deactivation.[21] Thus, our data helps gain fundamental understanding on a previously unrecognized deactivation mechanism, and on the activity of single-atom species for methane combustion.

Emission-limited decomposition kinetics

To further understand trends in the observed density-dependent particle decomposition, we analyzed the behavior of catalysts with smaller (2.5±0.4 nm) and larger (14.7±1.5 nm) diameter Pd nanoparticles, synthesized using the same colloidal strategies to independently tune particle size and density (Fig. 3a–c, Supplementary Fig. S2). For each size, reaction conditions were chosen in order to maintain similar conversion (~85%) before aging. The same density-dependent stability phenomenon, with the trend of denser catalysts being more stable, was observed for all sizes after an aging treatment performed in diluted oxygen at

775 °C (Supplementary Fig. S6). Although at higher density, an increase in particle size was observed in the 2.5 nm samples, there was significantly worse deactivation for the sample with lowest particle density, where EXAFS analysis revealed highly dispersed Pd species (Supplementary Fig. 7). This result highlights that the formation of atomically dispersed Pd species can be a more detrimental deactivation mechanism to methane combustion catalytic activity than the loss of surface area via particle aggregation. In the case of the largest 14.7 nm Pd particles, the trend of deactivation in lower particle density samples is still observed, but is much less severe than in the case of 2.5 and 7.9 nm Pd particles.

Interestingly, when different nanoparticle sizes at the same Pd loading were sequentially aged at increasing temperature, we found that the minimum temperature required to observe nanoparticle decomposition varied with size: smaller particles required lower temperatures (<600 °C), while larger particles required much higher temperatures (>700 °C) (Fig. 3d–f). This size dependence strongly suggests that the atomic ripening process is limited by atomic emission rather than surface diffusion of atomic species to a nearby site, the latter process being independent of the initial nanoparticle size. Previous work has also predicted noble metals to operate in this regime[22]. The increased stability of larger particles, caused by lower rates of adatom emission, can be due to lower surface energy, which decreases the energy of adsorbate formation (Supplementary Fig. 8)[23]. This analysis presents experimental proof that controlling the rate of atomic emission and adsorption to the support is key to limiting atomic redispersion or growth processes in many supported catalysts.

Thermodynamics of density-dependent nanoparticle decomposition

Different aging treatments at 775 °C were performed on the intermediate density 7.9 nm Pd/Al_2O_3 sample to understand the conditions that trigger nanoparticle decomposition (Fig. 4a). When aged in pure Ar, or Ar saturated with 10 vol. % H_2O, the catalyst actually showed minor improvements in activity, likely due to reconstruction of the Pd facets at high temperature. However, when aged in diluted O_2, the activity drop was substantial, and further deactivation was observed when aging in methane combustion conditions, or in a combination of O_2 and 10 vol. % H_2O. As γ-Al_2O_3 alone releases significant water (adsorbed during exposure to air) via dehydration and dehydroxylation processes when heated (Supplementary Fig. 9), directly co-feeding H_2O is not necessary for catalyst deactivation[24]. Furthermore, temperature-programmed reduction experiments in either Ar or O_2 demonstrate that it is likely the PdO phase which is present in during the activity loss accompanying nanoparticle decomposition (Fig. 4b). Past work has indeed suggested the PdO phase to be highly sensitive to the binding of H_2O[25]. These experiments demonstrate that O_2 and H_2O are both required to observe the particle decomposition and catalyst deactivation phenomenon, which are conditions commonly found in many catalytic environments.

Given that size-dependence studies identify atomic Pd emission, and not Pd surface diffusion, as the rate-determining step of the nanoparticle decomposition process, the chemical nature of the involved Pd atomic adsorbates was further investigated. To understand which Pd species are responsible for this unexpected deactivation, DFT calculations were performed considering Pd, PdO, and $Pd(OH)_2$ as adsorbates on (100) and

(110) γ-Al_2O_3 surfaces, including experimentally relevant temperature-dependent H_2O coverages (Supplementary Figure 10). In these calculations, only molecular species with one Pd atom were considered due to direct observation of Pd single atoms and lack of Pd-Pd coordination in EXAFS analysis of post-aging samples (Supplementary Table 2). Free energies of adsorption of various metal adatom complexes (ΔG_{ads}) were calculated, and referenced to 7.9 nm PdO particles, as temperature-programmed reduction experiments revealed that PdO is likely the phase present during particle decomposition (Fig. 4b). On both γ-Al_2O_3 surfaces, single Pd atoms have the least favorable adsorption energy (>1.5 eV uphill), and therefore likely do not constitute the emitted species - in line with the fact that aging in Ar, which converts PdO to Pd above 500 °C, does not cause deactivation (Fig. 4a). Instead, DFT reveals the existence of a lowest-energy $Pd(OH)_2$ adsorbate atop tri-coordinated Al atoms (Al_{III} defect sites, Fig. 5a,b), with an energy of adsorbate formation ΔG_{ads} ~0.5 eV uphill. Note that for temperatures up to 700 °C, $Pd(OH)_2$ adsorption energies are independent of temperature, as at these temperatures a hydrated Al_2O_3 surface is most stable. Above 700°C, a dehydrated Al_2O_3 surface is most stable, at which point we see a temperature dependent adsorption energy. These Al_{III} sites are common to the Al_2O_3(110) facet, which constitutes ~80% of the support surface, and are the same sites identified by Sautet *et al.* as reactive for CH_4 and H_2 splitting and N_2 adsorption.

Provided an understanding of the defect site and atomic emission energetics, we apply statistical mechanics to explain the observed density-dependent stability phenomenon. At an aging temperature of 775 °C, we expect nearly all Al_{III} sites (~1.5 sites nm^{-2}) to be free of H_2O and accessible for Pd atoms, although we still consider the possibility of site densities between 0.75 sites nm^{-2} and 1.5 sites nm^{-2}. Given an Al_{III} site density and the energy of adsorbate formation ΔG_{ads} (eV), the fraction of Pd atoms occupying Al_{III} defect sites ($<X_{Pd(OH)2}>$) is calculated according to a Boltzmann distribution (Eq. 1). This equation is plotted in Fig. 5c.

$$\left\langle X_{Pd(OH)_2} \right\rangle = \frac{\frac{N_{Al_{III}}}{N_{Pd}} e^{-\frac{\Delta G_{ads}}{KT}}}{\frac{N_{Al_{III}}}{N_{Pd}} e^{-\frac{\Delta G_{ads}}{KT}} + 1} \quad \text{Eq 1:}$$

Similar equations were recently derived using particle mass balances to find equilibrium concentrations of atomic adsorbates in traditional ripening processes[26,27]. Importantly, this analysis holds independent of the specific nature of the defect sites - the Boltzmann distribution always dictates larger equilibrium populations of single atom species formed at higher Al_{III} defect site (N_{Al_III}) to total Pd atom (N_{Pd}) ratios. Despite the single-atomic Pd adsorbate sites being higher in energy, samples with a lower particle density populate a larger fraction of Pd in the defect sites at increasing temperature because of the larger N_{Al_III}/N_{Pd} ratio in these materials (Fig. 5c). This system is a case where the formation of single sites is driven by entropy due to a large quantity of defect sites, rather than by enthalpy, which would be the case if adsorption energies were favorable. This is unique compared to many cases of metal single-sites trapped in reducible oxide supports, where favorable formation energy calculations suggest strong-binding sites[28]. Importantly,

consistent with this thermodynamic model, when the aged sparse sample is given long times and moderate temperatures (~10 hrs, 460 °C), atoms recondense into small nanoclusters, and activity slowly begins to return (Supplementary Fig. 11).

The insights gained from the work have important impacts for realistic powder catalysts synthesized by traditional impregnation approaches. To demonstrate that the severity of nanoparticle decomposition is not overstated in the use of monodisperse catalysts, we synthesize artificially polydisperse materials, prepared by mixing NPs of different sizes (Supplementary Fig. 12). These materials exhibit the same strong density-dependent stability, with the highest loaded material maintaining near complete activity, while the sparsest catalyst loses >75% of its CH_4 conversion. Additionally, we pursued conditions in which we observe nanoparticle growth in the dense catalyst; eventually, after 1000 min (17 h) the dense Pd/Al_2O_3 catalyst indeed forms larger aggregates (Supplementary Fig. 13), and sees loss of activity. However, the same loss of activity occurs in the sparse catalyst after only 10 minutes, due to nanoparticle decomposition. In other words, nanoparticle decomposition effects the same loss of activity as nanoparticle growth, but at a time-scale one hundred times quicker. The fact that the sample with dense Pd nanoparticle distribution shows particle growth after long-term aging is in line with atomic emission processes occurring for all samples, but with different consequences set by the dynamics involving equilibria between Pd atoms in alumina defects and in nanoparticles (Supplementary Fig. 14).

Across nanoparticle sizes, metals, and supports, colloidally synthesized catalysts with controllable nanoparticle density represent a general tool to reveal sintering and deactivation mechanisms in powder catalysts. Here, we report for the first time the dramatic effects of a novel deactivation mechanism that occurs at low particle loadings, demonstrating that the rapid formation of atomically dispersed catalysts may cause severe deactivation for certain reactions. Additionally, increasing nanoparticle loading was demonstrated to reduce the deactivating effects of nanoparticle decomposition and trapping as atomic species. The demonstrated atomic emission further suggests that eventual growth in particle size is due to atomic ripening, rather than particle migration processes.

METHODS

Synthesis of Colloidal Nanoparticles.

All syntheses were performed with standard air-free Schlenk techniques using previously published procedures[13,29]. $Pd(acac)_2$ (35% Pd, Acros Organics) was used as the metal precursor; 1-octadecene (ODE, 90%, Acros Organics), 1tetradecene (TDE, 94%, Alfa Aesar), and 1-dodecene, (DDE, 93–95%, Acros Organics) were used as solvents; 1-oleylamine (OLAM 70%, Aldrich), oleic acid (OLAC 90%, Aldrich), and trioctylphosphine (TOP, 97%, Aldrich) were used as surfactants and reducing agents. All chemicals were used as received. The general synthetic methodology is as follows: $Pd(acac)_2$ was added to a three-neck flask together with solvents, oleylamine, and oleic acid at room temperature. The mixture was evacuated for 15 min (<270 Pa), TOP was added, and the mixture was degassed for another 30 minutes at 50 °C. At this point, all solutions were a pale translucent light yellow. The reaction was flushed with nitrogen and quickly heated (~40 °C min^{-1}) to the

desired reaction temperature. After 15 minutes of reaction at the appropriate reflux temperature under vigorous magnetic stirring, the solution was allowed to cool to room temperature.

The exact amounts of reagents used to prepare the different sizes are as follows:

- 3.3 nm Pd particles: 157 mg of $Pd(acac)_2$; 11 mL of DDE; 9 ml of TDE; 1.64 mL of OLAM; 570 μL of TOP; degas at 50 °C for 30 mins; reaction at 230 °C for 15 mins under nitrogen.
- 8.8 nm Pd particles: 157 mg of $Pd(acac)_2$; 6.8 ml of TDE; 13.2 mL of ODE; 3.4 mL of OLAM; 0.8 mL of OLAC; 2.4 mL of TOP; degas at 50 °C for 30 mins; reaction at 290 °C for 15 mins under nitrogen.
- 16.2 nm Pd particles: 77 mg of $Pd(acac)_2$; 5 mL of ODE; 5 mL of OLAC; 0.56 mL of TOP; degas at 60 °C for 30 mins; reaction at 280 °C for 5 mins under nitrogen.

The particles were isolated by precipitation with addition of isopropanol, ethanol, and methanol and centrifugation (838 rad/s, 3 min), and were redissolved in hexanes. This procedure was repeated three times, after which the particles were dissolved in ~5 mL hexanes, with the addition of ~20 μL of oleylamine to ensure colloidal stability. For further size-selective purification of 16.2 nm particles, 1 mL aliquots of isopropanol were added to the black colloidal solution, followed by centrifugation at 838 rad/s, until the majority of particles precipitated, leaving a slightly grey supernatant. The supernatant was discarded, the precipitated was redispersed in hexanes, and the procedure was repeated 2 more times. Finally, the larger Pd NPs were dispersed in ~ 5 mL hexanes with ~20 μL of oleylamine to ensure colloidal stability.

Synthesis of Supported Catalysts.

Metal concentrations of synthesized colloidal nanoparticle solutions were determined via thermogravimetric analysis (TGA). A nanoparticle solution was added dropwise into an aluminum TGA pan, which was heated via hot plate at ~80 °C until 150 μL had been added. This pan was then heated in the TGA in flowing air up to 500 °C, and held until a steady mass was reached, indicating complete removal of solvents and organics. Dividing this final mass by the volume of solution added gave metal concentration. Using serial dilution, an appropriate amount of nanoparticles was dispersed in hexanes and added to a dispersion of ~2g support stirred in hexanes. For a given nanoparticle size, the same nanoparticle batch was used for all catalysts to ensure targeted metallic loadings and identical nanoparticle size and morphology across different weight loadings. Complete adsorption occurred immediately, but the solutions were left stirring for 1 hour. The solid was recovered by centrifugation (838 rad/s, 1 min) and dried at 60 °C overnight. Prior to catalytic tests, all samples were sieved below 180 μm grain size, fast-treated at 700 °C for 30 s in a furnace to remove ligands from synthesis as previously described and sieved again below 180 μm grain size[11]. Particle size distributions analysis after rapid thermal treatment demonstrated that particle size distributions were maintained compared to the original colloidal nanoparticles but that nanoparticle sizes were slightly smaller after deposition, probably due to removal of

organic impurities from the nanoparticles after the fast thermal treatment (Supplementary Fig. 2).

Microscopy Characterization Techniques.

Low-magnification transmission electron microscopy (TEM) was performed on a Tecnai operating at 200 kV. Scanning transmission electron microscopy (STEM) data was collected using a FEI Titan electron microscope equipped with an aberration-corrector for the probe-forming optics. The microscope was operated at an accelerating voltage of 300 kV and the convergence angle was ≈14 mrad. High-angle annular dark field (HAADF) images were collected with a Fischione Model 3000 annular detector using a camera length that set to the inner collection angle to ≈71 mrad. Samples were prepared by drop-casting dilute nanoparticle solutions or isopropanol dispersions of powder catalysts directly onto carbon-coated Cu grids. Particle size distributions were calculated by measuring >100 nanoparticle diameters, by hand, using ImageJ software[30].

X-ray Absorption Spectroscopy.

X-ray absorption spectra were collected at the Stanford Synchrotron Radiation Lightsource (SSRL, California, USA) at wiggler beamline 9–3 using a Si(220) double-crystal monochromator. The storage ring was operated at 3 GeV with a ring current of 494–500 mA in top-up mode. Data were collected at the Pd K-edge (24350 eV) in fluorescence mode using 32 and 100-element liquid nitrogen-cooled Ge detectors (Canberra). Catalysts were investigated as self-supporting pellets with an absorption length that prevented self-absorption at the Pd edge. A Pd reference foil was scanned simultaneously for energy calibration. The raw data were energy-calibrated, merged, and normalized using the Athena interface of the Demeter software package. The X-ray absorption fine structure (EXAFS) was extracted in k-space and the k3-weighted EXAFS function was used for Fourier-transformation. Phase shifts and amplitudes for relevant back-scattering paths were calculated using FEFF6. EXAFS modeling was carried out taking into account k1, k2, and k3-weighting using the Artemis interface of the Dimeter software. S02 was calculated to be 0.81 ± 0.04 by fitting Pd foil. The EXAFS data from all catalysts of a given Pd starting size were fit simultaneously to minimize errors.

X-ray Photoelectron Spectroscopy.

X-ray Photoelectron Spectra were measured using a PHI VersaProbe 3 Scanning XPS Microprobe equipped with a hemispherical electron analyzer using Al(Kα) radiation (1486.3 eV). All samples were deposited onto conductive carbon tabs on top of an aluminum holder, and were outgassed at 10^{-2} Pa and transferred to the ion-pumped analysis chamber. Pressure was kept below ~5×10^{-7} Pa throughout data acquisition. For most samples, the incident X-ray spot size was 100 um, and an excitation of 100 W at 20 kV was used. For all samples, a pass energy of 280 eV was used. An Ar^+ neutralizer and electron flood gun were used to compensate for Al_2O_3 charging, and binding energies (BE) were referenced to the C 1s peak (284.8 eV) to account for small charging effects.

Catalytic Characterization.

Due to the high temperatures required for this reaction and aging, Al_2O_3 was calcined at 900 °C for 24 h prior to Pd NP impregnation, to minimize support changes throughout reaction and aging. In general, each catalyst, post-ligand removal, was sieved below 180 μm grain size and mixed with a certain amount of Al_2O_3 diluent, which was found to be sufficient to eliminate thermal effects by repeated tests. 200 mg of this diluted mixture was loaded into the reactor to give a bed length of about 1.0 cm. When comparing stability across catalyst weight loadings for a given nanoparticle size, testing was performed under conditions such that each reactor bed had the same mass of Pd. For example, 200 mg of 0.007 wt. % Pd/Al_2O_3 was compared to a bed of 20 mg of 0.067 wt. % Pd/Al_2O_3 mixed with 180 mg Al_2O_3 diluent. This bed rested between two layers of granular quartz which were used for preventing displacement of the catalyst powder and for preheating the reactant gases. The reactor was heated by a square furnace (Micromeritics) and the temperature of the catalyst was measured with a K-type thermocouple inserted inside the reactor, touching the catalytic bed. All experiments were conducted at a total pressure of one atmosphere. Aging experiments consisted of an oxidative pretreatment (45 mL min^{-1} 5 vol. % O_2/Ar) at 275 °C to remove residual carbon compounds from synthesis, and to activate the catalyst. Next, the catalyst was ramped in 0.5 vol % CH_4, 4.0 vol % O_2, bal Ar to 460 °C at 20 °C min^{-1} and held until activity was stable. CH_4 was removed from the reaction mixture, and the catalyst was ramped to 775 °C at 20 °C min^{-1}, held for 1 hr, and ramped back to 460 °C at 20 °C min^{-1}, at which point CH_4 was reintroduced into the reaction mixture. Stability was assessed by comparing conversion before and after the aging procedure.

Analysis of Particle Density.

Voronoi analyses were performed using the Voronoi function in Matlab software. In this work, we study supported monodisperse 2.5 nm, 7.9 nm, and 14.7 nm Pd nanoparticles on γ-Al_2O_3 with a surface area of 96 m^2 g^{-1}. We simulate Al_2O_3 'grains' with nanoparticles impregnated onto the grain surface. Nanoparticles (1D points) were randomly generated on the surface of a grain as 2D uniformly-distributed random variables. In each simulated Pd/Al_2O_3 composite, input parameters included number of points (nanoparticles) and surface area of the Al_2O_3 (grain surface area). For a system with n nanoparticles, an $n \times n$ matrix of all interparticle distances was calculated. For each nanoparticle, the minimum distance to a nearest neighbor nanoparticle was selected, known as the nearest neighbor distance (NND). By averaging nearest neighbor distances across the entire grain, we calculated the average expected nearest neighbor distance. For each nanoparticle density, we simulated a large enough grain such that NP densities and nearest neighbor distances converge. However, by recording all NND and cell area values, we tally a distribution of these values.

Computational tools.

Density Functional Theory (DFT) calculations were performed with the software-package VASP 5.4[31–35] and the projector-augmented wave (PAW) method using standard PAWs and the functional PBE[36] with the zero damping DFT-D3 method of Grimme[37]. An energy cut-off of 400 eV and Gaussian smearing with a width of 0.1 eV was used in all calculations. The cell-parameters of γ-Al_2O_3 were optimized using an increased cut-off of 800 eV and

the optimized lattice constants are: a=5.593 Å, b=8.416 Å and c=8.075 Å. The structure is based on the model employed by Digne et al[38]. A **Γ**-centered (4×3×1)-k-point mesh was used for the γ-Al_2O_3 (100) surface and (2×2×1) for the γ-Al_2O_3 (110). The surfaces are modeled as 8-layer slabs separated by 16 Å vacuum. The 5 lowest layers were kept frozen. The calculations were carried out spin-polarized for PdO and $Pd(OH)_2$, but the most stable adsorbate structure show no spin polarization, and unpolarised for Pd and PdO_2. The nudge elastic band method (NEB) was used to determine the migration paths and barriers of the adsorbates on the surface. As reference values for PdO bulk $\Delta_fH°=-1.217$ eV[39] is used and the temperature dependent chemical potential calculated according to: $\Delta(\text{PdO bulk}) = \Delta_fH° - 0.5\ \mu_{O2}(T)$. The Gibbs free energy of O_2 and H_2O depending on the temperature and their partial pressures were calculated in the ideal gas approximation using the Atomic simulation environment (ASE)[40]. Due to the DFT uncertainty, all adsorption energies are corrected using Coupled Cluster (CC) calculations with the def2-QZVPP basis set on the CCSD(T) level of theory with Turbomole 7.1. (TURBOMOLE V7.1 2016, a development of University of Karlsruhe and Forschungszentrum Karlsruhe GmbH, 1989–2007, TURBOMOLE GmbH, since 2007; available from http://www.turbomole.com) by comparison of the adsorption energies of Pd, PdO and $Pd(OH)_2$ on $AlOH_3$+H_2O. $AlOH_3$+H_2O is a good model of the γ-Al_2O_3 surfaces because of similarities in the adsorption structures. The correction decreases the stability of Pd and increases the one of PdO and $Pd(OH)_2$. Also the formation energies ΔE_{form} of PdO, PdO_2 and $Pd(OH)_2$ from the gas-phase are calculated using the CCSD(T) level of theory and the def2-QZVPP basis set including spin polarization. The following values are used: $\Delta E_{form}(\text{PdO})=0.17$ eV, $\Delta E_{form}(PdO_2)=1.15$ eV and $\Delta E_{form}(Pd(OH)_2)=-1.61$ eV. Due to the low adsorption energy and the high energy of formation of PdO_2 compared to PdO und $Pd(OH)_2$ on the γ-Al_2O_3 (100) surface, PdO_2 was not considered as migration species and thus no barriers, correction factor or adsorption energy on γ-Al_2O_3 (110) calculated.

Data availability.

The datasets generated during and/or analysed during the current study are available from the corresponding author on reasonable request.

Supplementary Material

Refer to Web version on PubMed Central for supplementary material.

Acknowledgements.

We gratefully acknowledge support from the U.S. Department of Energy, Office of Sciences, Office of Basic Energy Sciences, through the SUNCAT Center for Interface Science and Catalysis. E.D.G. acknowledges support from the National Science Foundation Graduate Research Fellowship under Grant DGE-1656518. M.C. acknowledges support from the School of Engineering at Stanford University and from a Terman Faculty Fellowship. Part of this work was performed at the Stanford Nano Shared Facilities (SNSF), supported by the National Science Foundation under award ECCS-1542152. Use of the Stanford Synchrotron Radiation Lightsource, SLAC National Accelerator Laboratory, is supported by the U.S. Department of Energy, Office of Science, Office of Basic Energy Sciences under contract No. DE-AC0276F00515. Dr. Oliver Mueller is thanked for beamtime assistance. We finally acknowledge support from the state of Baden-Württemberg, Germany through bwHPC (bwunicluster and JUSTUS, RV bw16G001 and bw17D011) and financial support from the Helmholtz Association.

References

1. Argyle MD & Bartholomew CH Heterogeneous Catalyst Deactivation and Regeneration: A Review. Catalysts 5, 145–269 (2015).
2. Bartholomew CH Mechanisms of catalyst deactivation. Appl. Catal. A Gen 212, 17–60 (2001).
3. Tollefson J Worth its weight in platinum. Nature 450, 334–335 (2007). [PubMed: 18004347]
4. Farrauto Robert J.. Low-Temperature Oxidation of Methane. Science 337, 659–661 (2012). [PubMed: 22879495]
5. Liu J, Ji Q, Imai T, Ariga K & Abe H Sintering-Resistant Nanoparticles in Wide-Mouthed Compartments for Sustained Catalytic Performance. Nat. Sci. Reports 1–8 (2017). doi:10.1038/srep41773
6. Prieto G, Zecevic J, Friedrich H, Jong K & Jongh P Towards stable catalysts by controlling collective properties of supported metal nanoparticles. Nat. Mater 12, 34–39 (2013). [PubMed: 23142841]
7. Prieto G, Meeldijk JD, De Jong KP & De Jongh PE Interplay between pore size and nanoparticle spatial distribution: Consequences for the stability of CuZn/SiO2methanol synthesis catalysts. J. Catal 303, 31–40 (2013).
8. Goodman ED, Schwalbe JA & Cargnello M Mechanistic Understanding and the Rational Design of Sinter-Resistant Heterogeneous Catalysts. ACS Catal. 7, 7156–7173 (2017).
9. Scott SL A Matter of Life(time) and Death. ACS Catal. 8, 8597–8599 (2018).
10. Hansen TW, Delariva AT, Challa SR & Datye AK Sintering of catalytic nanoparticles: Particle migration or ostwald ripening? Acc. Chem. Res 46, 1720–1730 (2013). [PubMed: 23634641]
11. Cargnello M et al. Efficient Removal of Organic Ligands from Supported Nanocrystals by Fast Thermal Annealing Enables Catalytic Studies on Well-Defined Active Phases. J. Am. Chem. Soc 137, 6906–6911 (2015). [PubMed: 25961673]
12. Monai M, Montini T, Gorte RJ & Fornasiero P Catalytic Oxidation of Methane: Pd and Beyond. Eur. J. Inorg. Chem 10.1002/ejic.201800326 (2018). doi:10.1002/chem.201801190
13. Willis JJ et al. Systematic Structure-Property Relationship Studies in Palladium-Catalyzed Methane Complete Combustion. ACS Catal. 7, 7810–7821 (2017).
14. Zhu G, Han J, Zemlyanov DY & Ribeiro FH The turnover rate for the catalytic combustion of methane over palladium is not sensitive to the structure of the catalyst. J. Am. Chem. Soc 126, 9896–9897 (2004). [PubMed: 15303844]
15. Schwartz WR & Pfefferle LD Combustion of Methane over Palladium-Based Catalysts: Support Interactions. J. Phys. Chem. C 116, 8571–8578 (2012).
16. Otto K, Haack LP & deVries JE Identification of two types of oxidized palladium on ??-alumina by X-ray photoelectron spectroscopy. Appl. Catal. B, Environ 1, 1–12 (1992).
17. Datye AK, Xu Q, Kharas KC & Mccarty JM Particle size distributions in heterogeneous catalysts : What do they tell us about the sintering mechanism ? Catal. Today 111, 59–67 (2006).
18. Kwak JH, Hu J, Mei D, Yi C & Kim DH Coordinatively Unsaturated Al 3+ Centers as Binding Sites for Active Catalyst Phases of Platinum on g -Al 2 O 3. 5208, 1670–1674 (2009).
19. Zhang Z et al. Thermally stable single atom Pt/m-Al2O3 for selective hydrogenation and CO oxidation. Nat. Commun 8, 16100 (2017). [PubMed: 28748956]
20. Newton MA, Belver-Coldeira C, Martínez-Arias A & Fernández-García M Dynamic in situ observation of rapid size and shape change of supported Pd nanoparticles during CO/NO cycling. Nat. Mater 6, 528–532 (2007). [PubMed: 17529970]
21. Peterson EJ et al. Low-temperature carbon monoxide oxidation catalysed by regenerable atomically dispersed palladium on alumina. Nat. Commun 5, 1–11 (2014).
22. Challa SR et al. Relating Rates of Catalyst Sintering to the Disappearance of Individual Nanoparticles during Ostwald Ripening. J. Am. Chem. Soc 133, 20672–20675 (2011). [PubMed: 22087502]
23. Campbell CT, Parker SC & Starr DE The Effect of Size-Dependent Nanoparticle Energetics on Catalyst Sintering. Science 298, 811–814 (2002). [PubMed: 12399586]

24. Huang W, Goodman ED, Losch P & Cargnello M Deconvoluting Transient Water Effects on the Activity of Pd Methane Combustion Catalysts. Ind. Eng. Chem. Res (2018). doi:10.1021/acs.iecr.8b01915
25. Schwartz WR, Ciuparu D & Pfefferle LD Combustion of methane over palladiumbased catalysts: Catalytic deactivation and role of the support. J. Phys. Chem C 116, 8587–8593 (2012).
26. Ouyang R, Liu J & Li W Atomistic Theory of Ostwald Ripening and Disintegration of Supported Metal Particles Under Reaction Conditions. J. Am. Chem. Soc 135, 1760–1771 (2013). [PubMed: 23272702]
27. Parker SC & Campbell CT Kinetic model for sintering of supported metal particles with improved size-dependent energetics and applications to Au on TiO 2 „ 110 …. Phys. Rev. B 75, 035430 (2007).
28. Bruix A et al. Maximum Noble-Metal Efficiency in Catalytic Materials : Atomically Dispersed Surface Platinum ** Angewandte. Angew. Chemie - Int. Ed 53, 10525–10530 (2014).
29. Wu L et al. Tuning Precursor Reactivity toward Nanometer-Size Control in Palladium Nanoparticles Studied by in Situ Small Angle X-ray Scattering. Chem. Mater 30, 1127–1135 (2018).
30. Schneider CA, Rasband WS & Eliceiri KW NIH Image to ImageJ : 25 years of image analysis. Nat. Methods 9, 671–675 (2012). [PubMed: 22930834]
31. Hu CH et al. Modulation of catalyst particle structure upon support hydroxylation: Ab initio insights into Pd13 and Pt13/γ-Al 2O3. J. Catal 274, 99–110 (2010).
32. Kresse G & Hafner J Ab initio molecular dynamics for liquid metals. Phys. Rev. B 47, 558–561 (1993).
33. Kresse G & Hafner J Ab initio molecular-dynamics simulation of the liquid-metal– amorphous-semiconductor transition in germanium. Phys. Rev. B 49, 14251–14269 (1994).
34. Kresse G & Furthmüller J Efficiency of ab-initio total energy calculations for metals and semiconductors using a plane-wave basis set. Comput. Mater. Sci 6, 15–50 (1996).
35. Kresse G & Furthmüller J Efficient iterative schemes for ab initio total-energy calculations using a plane-wave basis set. Phys. Rev. B - Condens. Matter Mater. Phys 54, 11169–11186 (1996).
36. Perdew JP, Burke K & Ernzerhof M Generalized gradient approximation made simple. Phys. Rev. Lett 77, 3865–3868 (1996). [PubMed: 10062328]
37. Grimme S, Antony J, Ehrlich S & Krieg H A consistent and accurate ab initio parametrization of density functional dispersion correction (DFT-D) for the 94 elements H-Pu. J. Chem. Phys 132, (2010).
38. Digne M, Sautet P, Raybaud P, Euzen P & Toulhoat H Use of DFT to achieve a rational understanding of acid-basic properties of γ-alumina surfaces. J. Catal 226, 54–68 (2004).
39. Nell J & O'Neill HSC Gibbs free energy of formation and heat capacity of PdO: A new calibration of the Pd-PdO buffer to high temperatures and pressures. Geochim. Cosmochim. Acta 60, 2487–2493 (1996).
40. Larsen AH, Mortensen JJ, Blomqvist J & Jacobsen KW The atomic simulation environment—a Python library for working with atoms. J. Phys. Condens. Matter 29, 273002 (2017). [PubMed: 28323250]

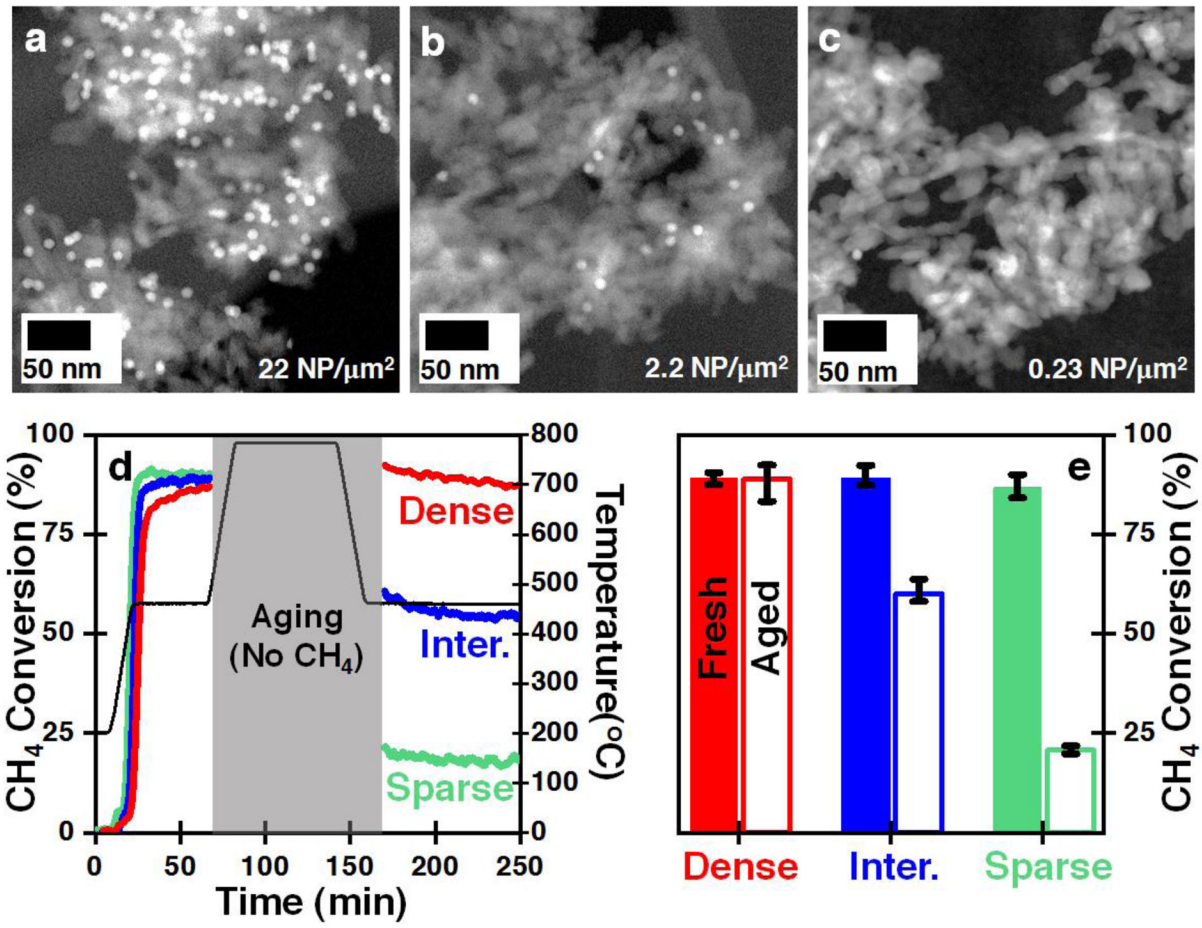

Fig. 1 |. Decoupling NP size and particle density demonstrate effects of NP spatial arrangement on catalytic stability.

Representative HAADF-STEM images of (a) dense (0.659 wt. %), (b) intermediate (0.067 wt. %), and (c) sparse (0.007 wt. %) Pd/Al_2O_3 samples. (d) CH_4 conversion profiles for Pd/Al_2O_3 catalysts with different nanoparticle loadings following the temperature profile (black line and secondary axis. (e) Averaged CH_4 conversion values at 460 °C for the Pd/Al_2O_3 catalysts before (Fresh) and after aging (Aged), where error bars represent the range of at least three repeat experiments.

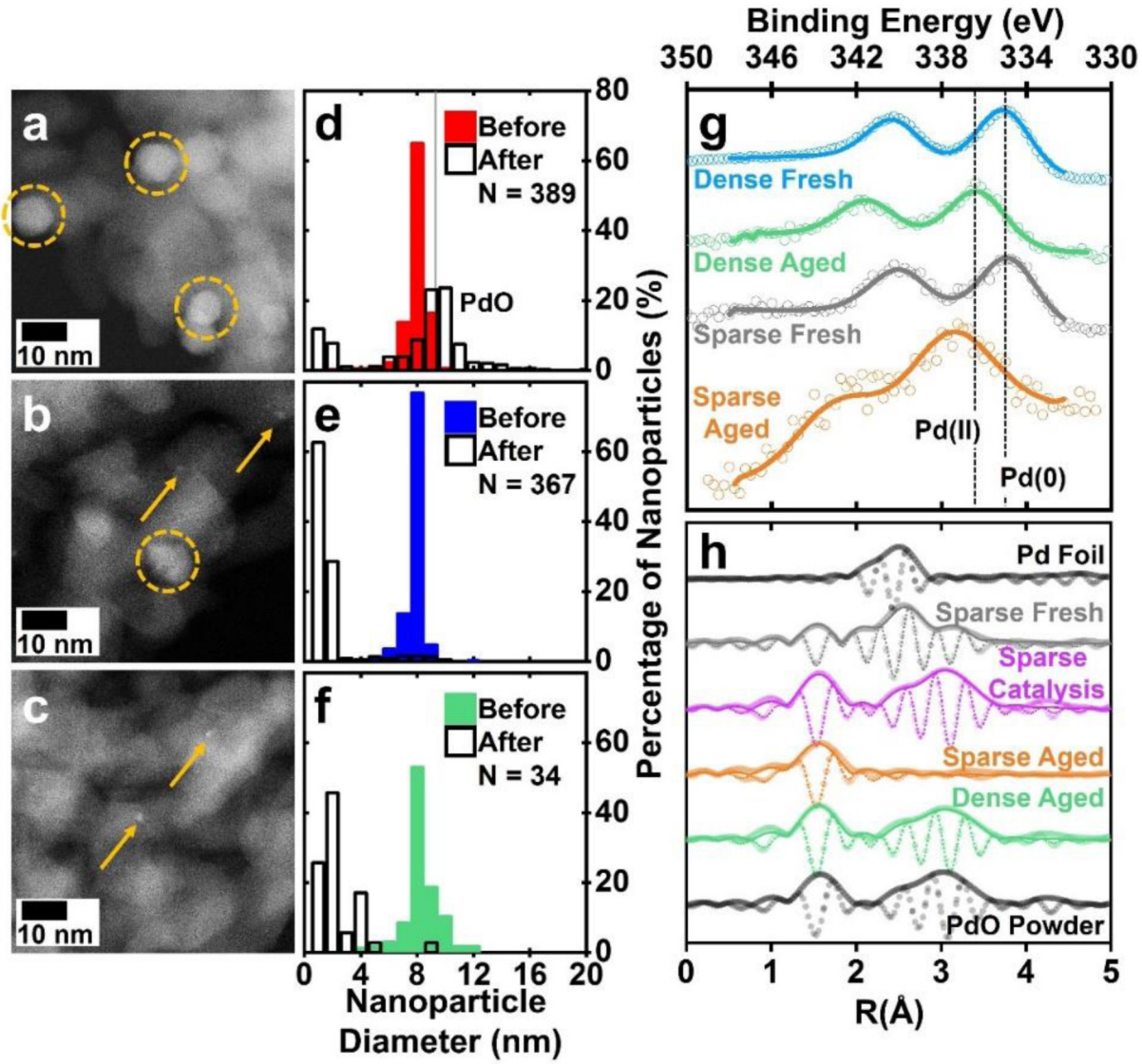

Fig. 2 |. Particle density-dependent conversion of Pd NPs into Pd single atoms.

Representative HAADF-STEM images of (a) dense, (b) intermediate, and (c) sparse Pd/Al_2O_3 samples after aging in 4 vol. % O_2/Ar for 1 h at 775 °C. Corresponding particle size distributions for the samples before and after aging for (d) dense, (e) intermediate, and (f) sparse catalysts. N indicates number of measurements made post-aging. (g) X-ray photoelectron spectra (XPS) of dense and sparse Pd/Al_2O_3 before (fresh) and after the aging treatment (aged). (h) Extended x-ray absorption fine structure spectra (EXAFS) of sparse and dense Pd/Al_2O_3 before (fresh), after catalysis at 460 °C (catalysis) and after the aging treatment (aged). Dark traces are fits, thicker light traces are experimental data. Solid traces are real components and dotted traces are imaginary components.

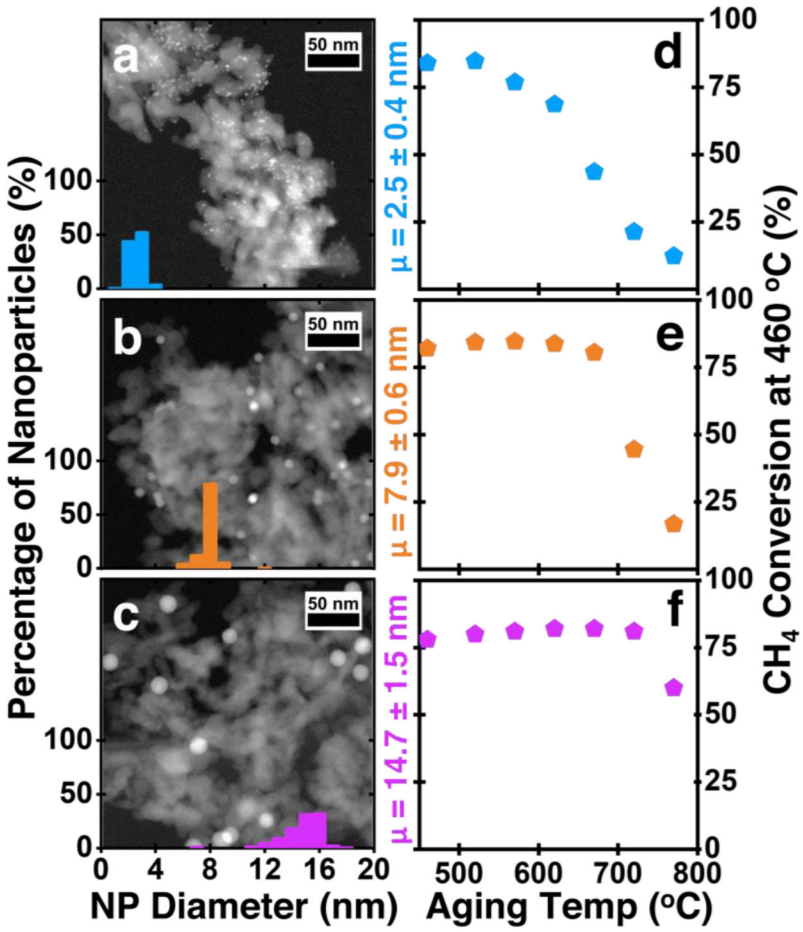

Fig. 3 |. Size control demonstrates interface-limited atomic emission.

HAADF-STEM images and particle size distributions (N = 200) of intermediate density Pd/Al_2O_3 catalysts with (a) 2.5 nm, (b) 7.9 nm, and (c) 14.7 nm Pd NPs. Temperature-dependent stability of sparse (g) 2.5 nm, (h) 7.9 nm, and (i) 14.7 nm Pd/Al_2O_3 catalysts. X-axis indicates the aging temperature before returning to catalysis conditions at 460 °C.

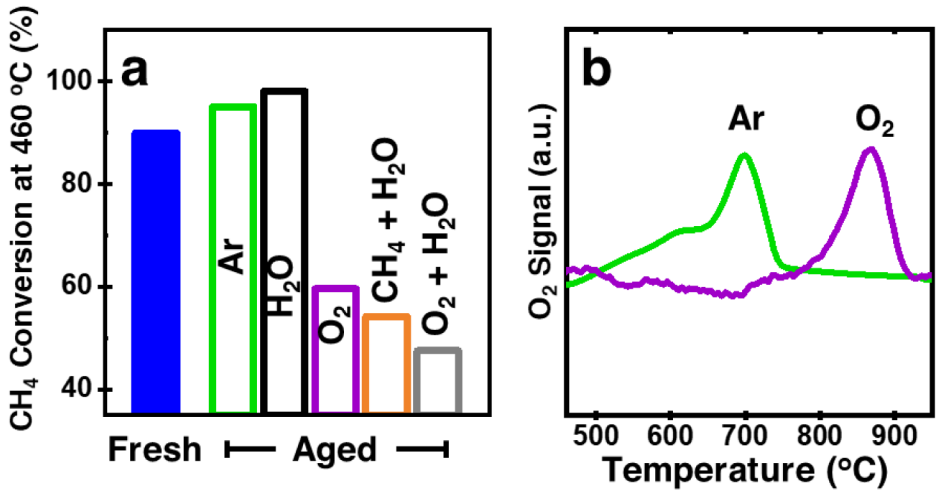

Fig. 4 |. Conditions of catalyst decomposition.

(a) Effect of aging in different environments at 775°C on stability of intermediate-density 7.9 nm Pd/Al_2O_3 catalyst. (b) Temperature-programmed oxygen evolution experiments on dense 7.9 nm Pd/Al_2O_3 catalyst.

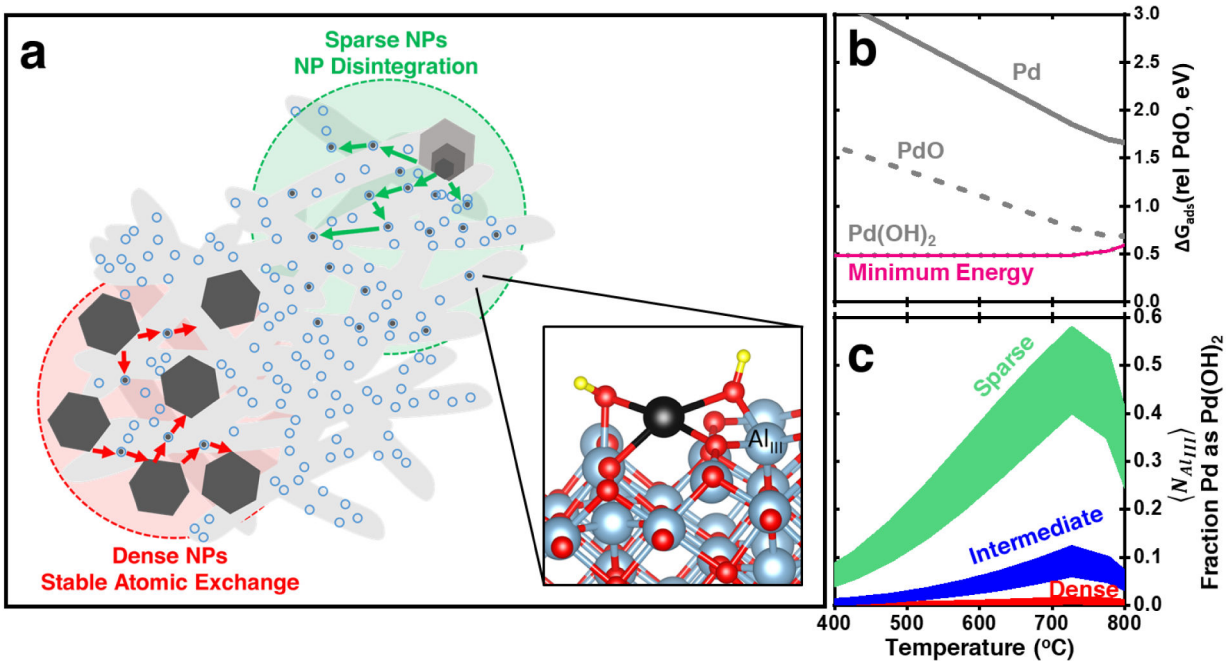

Fig. 5 |. Statistical mechanics model of density-dependent particle decomposition.

(a) Schematic illustrating the density-dependence of atomic redispersion. Open blue circles represent empty Al_{III} defect sites, and filled blue circles represent Al_{III} defect sites populated by Pd atomic species. Insert: most stable adsorbate structure showing $Pd(OH)_2$ binding to an Al_{III} site. (b) Energies of adsorbate formation of various atomic Pd species on the γ-Al_2O_3(110) surface, calculated by density functional theory. Energies are referenced to adsorption on a 7.9 nm PdO nanoparticle, and calculated using partial pressures of p_{O2} = 4000 Pa and p_{H2O} = 10400 Pa. (c) Fraction of Pd in Al_{III} defects as a function of temperature and NP density, according to Eq. 1, using temperature-dependent energies in (b). Band widths correspond to model sensitivity towards various alumina defect site densities (.75/nm^2 to 1.5/nm^2).